

IDENTIFICATION OF A JET-DRIVEN SUPERNOVA REMNANT IN THE SMALL MAGELLANIC CLOUD: POSSIBLE EVIDENCE FOR THE ENHANCEMENT OF BIPOLAR EXPLOSIONS AT LOW METALLICITY

LAURA A. LOPEZ^{1,5,6}, DANIEL CASTRO¹, PATRICK O. SLANE², ENRICO RAMIREZ-RUIZ³, CARLES BADENES⁴

Accepted by ApJ

ABSTRACT

Recent evidence has suggested that the supernova remnant (SNR) 0104–72.3 in the Small Magellanic Cloud (SMC) may be the result of a “prompt” Type Ia SN based on enhanced iron abundances and its association with a star-forming region. In this paper, we present evidence that SNR 0104–72.3 arose from a jet-driven bipolar core-collapse SN. Specifically, we use serendipitous *Chandra X-ray Observatory* data of SNR 0104–72.3 taken due to its proximity to the calibration source SNR E0102–72.3. We analyze 56 Advanced CCD Imaging Spectrometer (ACIS) observations of SNR 0104–72.3 to produce imaging and spectra with an effective exposure of 528.6 ks. We demonstrate that SNR 0104–72.3 is highly elliptical relative to other nearby young SNRs, suggesting a core-collapse SN origin. Furthermore, we compare ejecta abundances derived from spectral fits to nucleosynthetic yields of Type Ia and core-collapse (CC) SNe, and we find that the iron, neon, and silicon abundances are consistent with either a spherical CC SN of a 18–20 M_{\odot} progenitor or an aspherical CC SN of a 25 M_{\odot} progenitor. We show that the star-formation history at the site of SNR 0104–72.3 is also consistent with a CC origin. Given the bipolar morphology of the SNR, we favor the aspherical CC SN scenario. This result may suggest jet-driven SNe occur frequently in the low-metallicity environment of the SMC, consistent with the observational and theoretical work on broad-line Type Ic SNe and long-duration gamma-ray bursts.

Subject headings: ISM: abundances — ISM: supernova remnants — Magellanic Clouds — X-rays: ISM

1. INTRODUCTION

Hundreds of supernovae (SNe) are discovered each year at optical wavelengths by dedicated surveys which focus on nearby galaxies (e.g., Law et al. 2009; Leaman et al. 2011). Despite their high frequency, these SNe are too distant to resolve the SN ejecta and the immediate surroundings of the exploded stars. Fortunately, supernova remnants (SNRs) offer a complementary means to study SN explosions and dynamics up close and in detail.

Currently, ~ 350 SNRs have been identified in the Milky Way (MW) and the Large and Small Magellanic Clouds (LMC and SMC, respectively) through multi-wavelength campaigns (e.g., Green 2009; Badenes et al. 2010). The morphologies and spectral characteristics of these SNRs provide crucial insights regarding the nature of SN explosions, the environments of progenitors, and the interactions of massive stars and their circumstellar media (e.g., Badenes et al. 2007; Lopez et al. 2009a, 2011; Vink 2012). In particular, study of SNRs will aid in addressing two outstanding issues in the literature: the progenitors of Type Ia SNe and the triggering mechanism of jet-driven explosions.

Regarding the former topic, it is currently debated whether the progenitor of Type Ia SNe is a single white dwarf accreting from a non-degenerate companion (e.g., Whelan & Iben 1973) or the merger of a double white-dwarf system (e.g. Iben & Tutukov 1984; Webbink 1984; Guillochon et al. 2010; Dan et al. 2012; Pakmor et al. 2012). Nearby Type Ia SNRs can be investigated for clues regarding the nature of the progenitors, including searches for a surviving non-degenerate companion (e.g., Schaefer & Pagnotta 2012; Kerzendorf et al. 2013) and evidence of a circumstellar medium modified by a non-degenerate companion (e.g., Williams et al. 2011).

Secondly, many mysteries remain regarding the nature of jet-driven SNe. Jet-driven core-collapse (CC) SNe are thought to occur among ~ 1 –2% of Type Ib/c SNe (Soderberg et al. 2010), and some fraction of these events are associated with long gamma-ray bursts (GRBs; e.g., Izzard et al. 2004; Podsiadlowski et al. 2004). As GRBs are typically detected at cosmological distances (see review by Gehrels et al. 2009), identification of local analogues among the nearby SNR population would help constrain the physics, dynamics, and nucleosynthesis of these explosions (e.g., Ramirez-Ruiz & MacFadyen 2010; Lopez et al. 2013a,b; González-Casanova et al. 2014).

Recently, it was reported that SNR 0104–72.3 in the SMC may be the remnant of an unusual Type Ia explosion (Lee et al. 2011). In particular, these authors showed that modeling of X-ray spectra from SNR 0104–72.3 required an overabundance of iron, consistent with a Type Ia origin for this SNR. As this source is also associated with a nearby star-forming region (e.g., Koo et al. 2007), Lee et al. concluded that the progenitor of SNR 0104–72.3 may have been a white dwarf from a young population of stars, i.e. from a “prompt” Type

lopez@space.mit.edu

¹ MIT-Kavli Institute for Astrophysics and Space Research, 77 Massachusetts Avenue, 37-664H, Cambridge MA 02139, USA

² Harvard-Smithsonian Center for Astrophysics, 60 Garden St., Cambridge, MA 02138, USA

³ Department of Astronomy and Astrophysics, University of California Santa Cruz, 1156 High Street, Santa Cruz, CA 95060, USA

⁴ Department of Physics and Astronomy and Pittsburgh Particle Physics, Astrophysics and Cosmology Center (PITT PACC), University of Pittsburgh, 3941 O’Hara St, Pittsburgh, PA 15260, USA

⁵ NASA Einstein Fellow

⁶ Pappalardo Fellow in Physics

Ia SN (e.g., Scannapieco & Bildsten 2005; Aubourg et al. 2008).

To further investigate the unusual nature of this SNR, in this paper we take advantage of serendipitous observations of SNR 0104–72.3 with the *Chandra X-ray Observatory*. Due to its close proximity ($\sim 11'$) to the *Chandra* calibration source SNR E0102–72.3, SNR 0104–72.3 has been observed regularly throughout the lifetime of *Chandra*. When combined, these data are nearly five times deeper than the targeted *Chandra* observations presented by Lee et al. (2011). Using these data, we present evidence that the SNR actually arose from a jet-driven CC SN. In Section 2, we detail the archival observations of SNR 0104–72.3 and how we merged these data. In Section 3, we utilize these combined data to explore the explosive origin of SNR 0104–72.3, based on its morphology (Section 3.1) and its metal abundances (Section 3.2). We present a discussion and conclusions in Section 4, with emphasis on the implication of finding a jet-driven CC SNR in the low-metallicity SMC.

2. DATA REDUCTION

We identified the available *Chandra* imaging of SNR 0104–72.3 using the following procedure. First, we searched the *Chandra* archive for ACIS-I and ACIS-S observations within $20'$ of SNR 0104–72.3 without gratings and in timed-exposure mode. This query yielded 242 observations: 237 calibration observations of SNR E0102–72.3, as well as pointed observations of SNR 0104–72.3 (ObsIDs 9100 and 9810), of the nearby SNR 0103–72.6 (ObsID 2758), and of the SMC wing (ObsIDs 5485 and 5486). Then, we visually inspected the 242 observations to identify all those where the entirety of SNR 0104–72.3 was imaged by an ACIS chip, regardless of off-axis distance. Using this strategy, we found 56 ACIS-I and ACIS-S observations of SNR 0104–72.3 from 2000–2009, with a combined integration of 528.6 ks. These observations are listed in Table 1 along with relevant details for each pointing, including the ACIS chip on which SNR 0104–72.3 is located, the off-axis distance of SNR 0104–72.3 to the aim point, and the net (background-subtracted) full-band (0.5–8.0 keV) counts obtained. The median off-axis distance of SNR 0104–72.3 in the 56 observations is $10'$. For reference, at 1.49 keV, the point-spread function⁷ is $\approx 6''$ at $10'$ off axis, small enough to resolve substructures in the $\sim 1.7'$ diameter SNR 0104–72.3. In the analyses described below, we use the software *Chandra* Interactive Analysis of Observations (CIAO) Version 4.3 and XSPEC Version 12.7.0 (Arnaud 1996).

We merged the imaging data using the CIAO command *reproject_image_grid*, which maps images into one reference frame. The resulting full-band (0.5–8.0 keV) *Chandra* image is shown in Figure 1. The net number of (background subtracted) full-band counts from the source in the merged observation is $\sim 3.1 \times 10^4$ counts, sufficient to perform spatially-resolved spectroscopic analysis and to distinguish line emission in the spectra. For comparison, the 110 ks targeted ACIS-S3 observations (ObsIDs 9100 and 9810) from Lee et al. yielded ~ 9500 net full-band

TABLE 1
OBSERVATIONS OF SNR 0104–72.3, SORTED BY OBSID

ObsID	Obs Date	Exposure (ks)	Chip ^a	Off-Axis Distance ^b	Net Counts ^c
1316	2000-12-15	6.87	S2	12.4	358
1317	2000-12-15	6.87	S2	14.4	357
1528	2000-12-16	6.87	I2	5.1	303
1544	2001-06-05	7.42	I1	5.6	398
2835	2001-12-05	7.83	I2	6.6	365
2836	2001-12-05	7.46	I2	8.0	342
2839	2001-12-05	7.46	S2	13.3	337
2841	2001-12-06	7.46	I2	5.2	410
2850	2002-06-19	7.76	I3	10.1	321
2852	2002-06-19	7.56	I2	10.3	298
2864	2002-06-21	7.56	I1	6.0	366
3529	2003-08-09	7.65	I1	8.4	259
3530	2003-08-09	7.65	I1	6.6	335
3531	2003-08-10	8.07	I1	4.7	314
3534	2003-08-10	7.66	I0	10.1	256
3536	2003-02-02	7.63	S3	12.3	576
3537	2003-02-02	7.63	S3	11.4	565
3538	2003-02-02	7.63	S3	14.2	551
3539	2003-02-02	7.63	S3	16.1	551
3540	2003-02-02	7.63	S3	18.0	497
3541	2003-02-02	7.63	I2	6.2	335
3542	2003-02-02	7.63	I3	8.8	315
3543	2003-02-02	7.64	S2	13.7	390
3544	2003-08-10	7.86	I2	10.7	249
3547	2003-08-08	7.66	I2	12.3	260
5130	2004-04-09	19.41	S4	10.0	891
5131	2004-04-05	8.01	S4	11.9	134
5132	2004-04-09	7.50	S2	4.1	431
5133	2004-04-09	7.50	S1	11.3	547
5134	2004-04-09	7.50	S3	6.2	611
5135	2004-04-10	8.14	S5	19.9	271
5143	2004-04-26	7.35	I1	8.2	308
5145	2004-04-28	7.15	I3	6.8	353
5150	2003-12-19	7.57	S2	12.7	353
5151	2003-12-19	7.57	S2	14.7	305
5153	2003-12-16	7.40	I2	5.1	254
6042	2005-04-12	18.90	S4	10.0	858
6043	2005-04-18	7.85	S4	11.9	344
6049	2004-12-13	7.58	I2	7.6	272
6050	2004-12-13	7.16	I2	8.5	260
6051	2005-01-12	17.92	S2	11.1	630
6053	2005-01-12	7.16	S3	14.8	460
6054	2005-01-12	7.17	S3	16.8	447
6056	2004-12-17	8.01	I2	5.2	224
6753	2006-03-14	7.17	I3	3.8	298
8361	2007-02-05	19.79	S3	11.4	1405
8362	2007-02-11	8.84	I2	5.1	391
8363	2007-02-11	8.45	I3	9.7	340
8364	2007-02-11	8.45	S2	13.0	248
9100	2008-01-27	54.47	S3	0.6	4762
9691	2008-02-04	7.94	I2	5.9	340
9692	2008-02-05	7.67	I3	9.0	245
9693	2008-02-05	7.68	S2	13.5	335
9810	2008-01-30	55.82	S3	0.6	4745
10650	2009-02-16	7.93	I2	4.4	350
10652	2009-01-17	8.07	S2	14.7	259

- ^a ACIS chip where SNR 0104–72.3 is located in the observation.
^b Angular distance in arcminutes from the observation aim point to the position of SNR 0104–72.3, at right ascension 01h06m14s and declination $-72d05m18s$ (J2000).
^c Total number of background-subtracted source counts in the 0.5–8.0 keV band during the observation.

counts (note that the count rates are different between observations depending on several factors, such as which ACIS chip imaged SNR 0104–72.3). We also produced narrow-band images at the energies of possible ejecta emission lines, but no unique structures/morphologies were evident, so we do not include them in this text.

⁷ Defined as the radius where 50% of encircled energy of a point source is detected: <http://cxc.harvard.edu/proposer/POG/html/index.html>

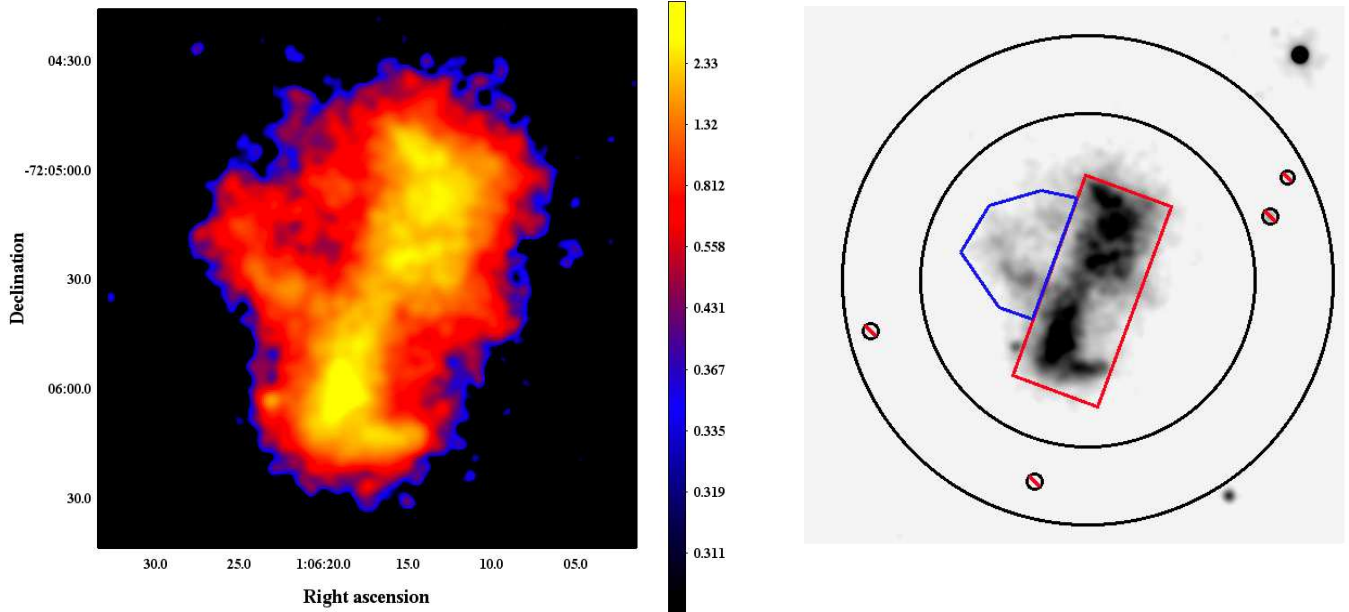


FIG. 1.— *Left*: Full-band (0.5–8.0 keV) *Chandra* image of SNR 0104–72.3 from the combined 528.6 ks data. Image has been smoothed with a 2.5'' Gaussian kernel. *Right*: Full-band image with regions of spectral extraction overplotted: the “bar” and the “arc” regions in red and blue, respectively, and the region used for background subtraction (inside the black annulus, with the four point sources excluded).

3. ANALYSES AND RESULTS

Using these archival data, we explore the explosive origin of SNR 0104–72.3, based on the X-ray morphology (Section 3.1) and on the ejecta metal abundances derived from X-ray spectral fits (Section 3.2).

3.1. Morphology

Recently, we have developed techniques to quantify the morphological properties of SNRs (Lopez et al. 2009b). We have applied these methods to archival *Chandra* and *Spitzer Space Telescope* images of young, ejecta-dominated SNRs ($\lesssim 25000$ years old) to measure the asymmetry of their thermal X-ray and warm dust emission (Lopez et al. 2009a, 2011; Peters et al. 2013). In these works, we found that the X-ray and IR morphology of SNRs can be used to differentiate Type Ia and CC SNRs. In particular, the thermal X-ray and IR emission of Type Ia SNRs are statistically more circular and mirror symmetric than that of CC SNRs. These results can be attributed to both the distinct geometries of the respective explosion mechanisms as well as the different circumstellar environments of Type Ia and CC SNe.

Here, we apply the same symmetry technique as used previously, the power-ratio method (PRM), to the merged *Chandra* soft-band (0.5–2.1 keV) image of SNR 0104–72.3. Qualitatively, the morphology of SNR 0104–72.3 appears bipolar in nature, but statistical comparison to a large sample of young SNRs reveals its distinctive nature. In this paper, we give a short overview of the PRM, and we refer the reader to our previous papers for the relevant background and equations.

The PRM quantifies asymmetries via calculation of the multipole moments Ψ_m of emission in a circular aperture. It is derived similarly to the expansion of a two-dimensional gravitational potential, except an image’s surface brightness replaces the mass surface density. The powers P_m are obtained by integrating the magnitude of

each term Ψ_m over the aperture radius R . We divide the powers P_m by P_0 (the first term of the expansion) to normalize with respect to flux, and we set the origin position of our aperture to the centroid of the image so that the dipole power ratio P_1/P_0 approaches zero. In this case, the higher-order terms reflect the asymmetries at successively smaller scales. We focus on the two ratios in particular: the quadrupole power ratio P_2/P_0 , which characterizes the ellipticity or elongation of a source, and the octupole power ratio P_3/P_0 , which quantifies the mirror asymmetry of a source.

We estimate the uncertainty in the power ratios of SNR 0104–72.3 using a Monte Carlo approach. The soft-band image of SNR 0104–72.3 was adaptively binned using the *AdaptiveBin* software (Sanders & Fabian 2001) to smooth out noise. Subsequently, noise was added back by taking each adaptive pixel’s intensity as the mean of a Poisson distribution and selecting a new intensity from that distribution. This process was repeated 100 times to produce 100 soft-band images of SNR 0104–72.3, and the 1σ confidence limits on P_2/P_0 and P_3/P_0 are given by the sixteenth highest and lowest power ratios derived from the 100 images.

Figure 2 plots the resulting quadrupole power ratio P_2/P_0 versus octupole power ratio P_3/P_0 for SNR 0104–72.3 compared to the values obtained for 24 galactic and LMC SNRs published in Figure 2 of Lopez et al. (2011). SNR 0104–72.3 falls in the CC SNR regime of the diagram, and it is the most elliptical and mirror asymmetric of all the sources, with $P_2/P_0 = 660 \pm 26$ and $P_3/P_0 = 67.7^{+3.8}_{-3.3}$. Thus, the X-ray morphology of SNR 0104–72.3 is suggestive of a CC explosive origin. Moreover, recent hydrodynamical simulations have shown that the X-ray morphologies of jet-driven CC SNRs retain their bipolar structures over many hundreds of years (González-Casanova et al. 2014). Thus, the extreme elongation and asymmetry of

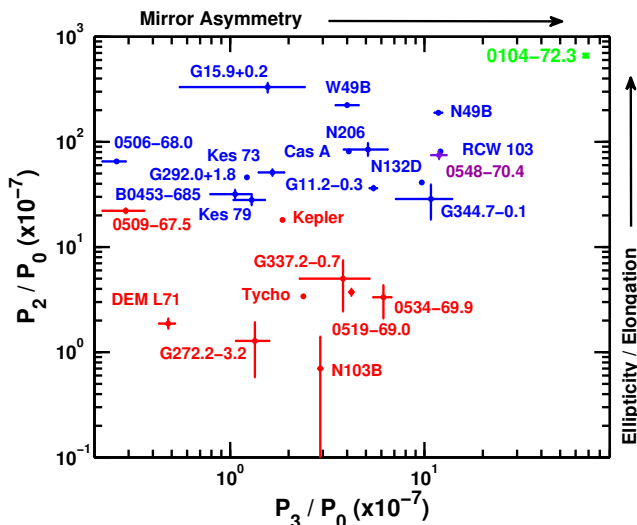


FIG. 2.— Results of the power-ratio method for SNR 0104–72.3 (plotted in green) compared to 24 galactic and LMC SNRs (adapted from Figure 2 of Lopez et al. 2011). The quadrupole power ratio P_2/P_0 measures ellipticity/elongation; the octupole power ratio P_3/P_0 quantifies mirror asymmetry. Type Ia SNRs are plotted in red, and the CC SNRs are in blue (based on their ejecta abundance ratios). One source, SNR 0548–70.4, is in purple because of its anomalous abundance ratios. SNR 0104–72.3 falls in the CC regime of the diagram. Furthermore, it is the most elliptical and mirror asymmetric of the sample, indicative of a complex environment and/or a highly bipolar explosion.

SNR 0104–72.3 is consistent with a bipolar, jet-driven CC origin.

3.2. Spatially-Resolved Spectroscopy

For our spectral analyses of SNR 0104–72.3, we extracted source and background spectra individually from each of the 56 ACIS observations using the CIAO command *specextract*. The regions of extraction are shown in Figure 1 (right panel), including two source regions (the “bar” in red and the “arc” in blue) and an annulus region around SNR 0104–72.3 (in black) used for the background.

We began by replicating the modeling of Lee et al. (2011) on their two pointed ACIS-S observations of SNR 0104–72.3 (ObsIDs 9100 and 9810). Due to an error in transcribing the SMC abundances from Russell & Dopita (1992), Lee et al. adopted incorrect abundances in their fits, affecting their derived parameters (J.-J. Lee, private communication). Thus, we first verified that we could obtain the same results as Lee et al. (2011) using identical data and models with their (incorrect) adopted SMC abundances, and subsequently, we adopted the actual Russell & Dopita (1992) SMC abundances to see how the fits changed. All uncertainties listed below are 90% confidence ranges for the given parameters.

We extracted spectra from the same two regions as Lee et al. (the bar and the arc), and we modeled the spectra as a single absorbed non-equilibrium ionization (NEI) plasma using the plane-parallel shock model *vpshock* in XSPEC (Borkowski et al. 2001). We accounted for both the foreground absorption by the Milky Way, $N_{\text{H,MW}}$, as well as the intrinsic absorption through the SMC, $N_{\text{H,SMC}}$, using the XSPEC model components *phabs* and *vphabs*, respectively. For

the former component, we fixed the column density to $N_{\text{H,MW}} = 2.2 \times 10^{20} \text{ cm}^{-2}$, the H I column density toward SNR 0104–72.3 (Dickey & Lockman 1990). We began fitting with $N_{\text{H,SMC}}$, the plasma temperature, and normalization thawed, and with all the metals of $N_{\text{H,SMC}}$ and the NEI plasma frozen to SMC ISM abundances. As in Lee et al., these fits produced large residuals in the 0.8–1.2 keV range. In this band, Ne K and Fe L lines are prominent, so we subsequently freed both of these parameters and refit the data.

Using this approach, we obtained best-fit parameters consistent within the uncertainties of the Lee et al. results for the bar and arc when using their SMC abundances. The results were similar whether we adopted Anders & Grevesse (1989) or Asplund et al. (2009) for solar abundances. Therefore, we interpret all discrepancies from the Lee et al. results in the rest of this paper as stemming from the incorrectly adopted SMC abundances. In all analyses below, we opted to use Asplund et al. (2009) for our solar abundance values.

We then remodeled the Lee et al. spectra but with the correct SMC abundances from Russell & Dopita (1992)⁸. In both the bar and the arc, the resulting best-fit models had large ionization timescales ($\tau \gtrsim 10^{13} \text{ s cm}^{-3}$), which are long enough for the plasma to have reached collisional ionization equilibrium (CIE: Smith & Hughes 2010). Consequently, we substituted the variable abundance collisional ionization equilibrium plasma component *vappec* v2.0.2 (Smith et al. 2001; Foster et al. 2012) for the *vpshock* component used above. Thus, written out in terms of XSPEC components, our model was $\text{phabs} \times \text{vphabs} \times \text{vappec}$.

In the bar region, we began with all metals frozen to SMC ISM abundances; this model was statistically poor (with $\chi^2 \approx 948$ with 94 degrees of freedom) due to large residuals in the 0.8–1.2 keV range. Therefore, we freed the Ne and Fe abundances, and the resulting fit (shown in Figure 3), improved dramatically, with $\chi^2/\text{d.o.f.} \approx 119/92$. We followed a similar procedure with the Lee et al. data for the arc region. With all metals frozen to SMC values, we obtained a fit with $\chi^2/\text{d.o.f.} \approx 110/46$. By thawing Ne and Fe and remodeling, the new fit improved statistically, with $\chi^2/\text{d.o.f.} \approx 57/44$. Moreover, we thawed the Si abundance due to a large residual just below 2 keV, near the centroid of the Si XIII line. This final fit, shown in Figure 3, gave $\chi^2/\text{d.o.f.} \approx 46/43$, and all of the best-fit parameter values and their associated 1- σ errors are listed in Table 2.

We find two noteworthy differences, in addition to the long ionization timescales, from the fits reported by Lee et al. (2011). First, we derive lower column densities, with $N_{\text{H,SMC}} = (4.5^{+3.5}_{-2.9}) \times 10^{21} \text{ cm}^{-2}$ in the arc and $N_{\text{H,SMC}} = (3.0 \pm 0.8) \times 10^{21} \text{ cm}^{-2}$ in the bar. These columns are slightly below the H I column density measured toward SNR 0104–72.3 of $\sim 6 \times 10^{21} \text{ cm}^{-2}$ by Stanimirovic et al. (1999), indicating the SNR may be on the nearer edge of the SMC. Secondly, we found that the arc may have enhanced abundances of Ne, Si, and Fe (as shown in Figure 3 and listed in Table 2), with

⁸ Relative to solar, the SMC abundances given in Table 1 of Russell & Dopita (1992) are as follows: He = 0.83; C = 0.15; N = 0.04; O = 0.13; Ne = 0.15; Mg = 0.25; Si = 0.30; S = 0.24; Ar = 0.18; Ca = 0.20; Fe = 0.15; Ni = 0.40.

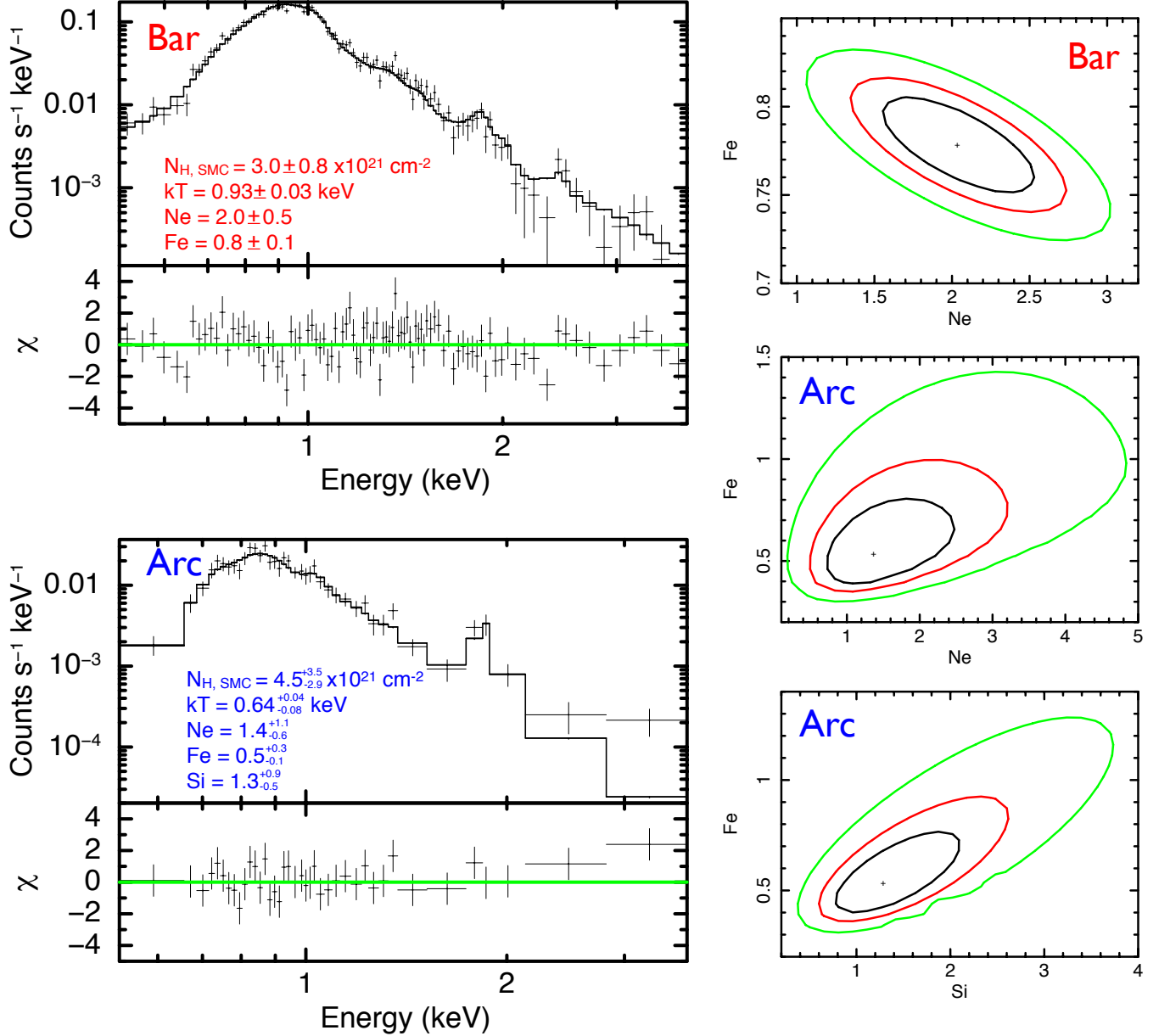


FIG. 3.— Spectral analyses of the bar and arc from the 110-ks pointed *Chandra* ACIS-S observations of SNR 0104–72.3. *Top left*: Spectra and model of bar region of the SNR. *Bottom left*: Same as top except for the bar region of SNR 0104–72.3. *Right panels*: 68%, 95%, and 99% confidence contours of Fe versus Ne abundances in the bar (top), of Fe versus Ne abundances in the arc (middle), and of Fe vs Si abundances in the arc (bottom). All abundances are relative to solar by number. In the bar, we find enhanced abundances of Fe and Ne, and in the arc, we find enhanced abundances of Ne, Si, and Fe in the arc, although the confidence limits do not exclude the SMC ISM abundance values there.

a Ne abundance of $1.4^{+1.1}_{-0.6}$, an Fe abundance of $0.5^{+0.3}_{-0.1}$, and a Si abundance of $1.3^{+0.9}_{-0.5}$ by number relative to solar. However, the confidence contours demonstrate that we cannot exclude the SMC ISM abundances (of 0.15 for both Ne and Fe and of 0.30 for Si) based on the 110 ks of pointed observation data. In the bar region, we also find statistically significantly enhanced abundances of Ne and Fe, with an Ne abundance of 2.0 ± 0.5 and an Fe abundance of 0.8 ± 0.1 . These elevated abundances are required to adequately fit the spectrum, indicating an ejecta origin of the emission in the bar.

Subsequently, we modeled the background-subtracted spectra from the 56 observations to derive stricter limits on these parameters. Initially, we attempted to model

the 56 individual spectra simultaneously of each region. However, this method did not yield reliable results, and the procedure often settled on parameters corresponding to local minima in chi-squared space, rather than the global minima. Therefore, we combined the spectra of the observations with SNR 0104–72.3 on front-illuminated (FI) chips (ACIS I0–I3, S0, S2, S4, and S5; 44 observations) and those on back-illuminated (BI) chips (ACIS S1 and S3; 12 observations). We selected this procedure because the FI and BI chips have different responses: the BI chips have better chip-averaged energy resolution and responses which extend to lower energies than the FI chips. To combine the data, we used the CIAO command *combine_spectra* to create FI and BI spectra

TABLE 2
 SPECTRAL RESULTS^a

Region	$N_{\text{H,SMC}}^{\text{b}}$ ($\times 10^{21} \text{ cm}^{-2}$)	kT (keV)	Ne ^c	Fe ^c	Si ^c	$\chi^2/\text{d.o.f.}$
Models of Pointed ACIS Observations of SNR 0104–72.3						
Bar	3.0 ± 0.8	0.93 ± 0.03	2.0 ± 0.5	0.8 ± 0.1	0.30	119/92
Arc	$4.5^{+3.5}_{-2.9}$	$0.64^{+0.04}_{-0.06}$	$1.4^{+0.1.1}_{-0.6}$	$0.5^{+0.3}_{-0.1}$	$1.3^{+0.9}_{-0.5}$	46/43
Models of All 56 ACIS Observations of SNR 0104–72.3						
Bar	2.8 ± 0.5	0.93 ± 0.02	$2.8^{+0.7}_{-0.5}$	0.8 ± 0.1	0.30	397/223
Arc	$4.8^{+3.0}_{-2.6}$	$0.66^{+0.04}_{-0.07}$	$1.6^{+0.5}_{-0.4}$	0.5 ± 0.1	0.9 ± 0.3	195/121

^a All error bars reflect 68% uncertainty ranges.

^b Intrinsic absorption through the SMC. Foreground absorption by the Milky Way was fixed to $N_{\text{H,MW}} = 2.2 \times 10^{20} \text{ cm}^{-2}$.

^c Abundances are relative to solar by number. The Si abundance of 0.3 in the bar is the SMC ISM value.

from the arc and bar (see Figure 4, left panels). Then, we modeled the FI and BI spectra simultaneously for each of the two regions. Following the presentation of our results below, we discuss the caveats associated with this approach.

For the arc region, we began with the abundances frozen to their SMC values, and we obtained a fit with $\chi^2/\text{d.o.f.} \approx 369/124$. We thawed the Ne and Fe abundances due to the large residuals from 0.8–1.2 keV, and the fit improved, with $\chi^2/\text{d.o.f.} \approx 213/122$. Motivated by the emission peak near ~ 1.8 keV, we thawed the Si abundance as well, and we obtained a fit with $\chi^2/\text{d.o.f.} \approx 195/121$ (shown in Figure 4 and listed in Table 2). This fit is statistically acceptable, but we note that the residuals above 2 keV are fairly large in the arc spectra. Due to the limited counts at those high energies, the nature of the excess flux is uncertain: it could be additional emission lines, a non-thermal component, or an additional hot thermal plasma component.

In the bar, we followed a similar procedure; the fit with the abundances frozen to the SMC values was especially poor, with $\chi^2/\text{d.o.f.} \approx 3074/225$. With Ne and Fe thawed, we obtained a fit with $\chi^2/\text{d.o.f.} \approx 397/223$, as shown in Figure 4 and listed in Table 2. The bar fit did not improve statistically with a thawed Si abundance, so we left it frozen to the SMC ISM abundance of 0.30 solar by number.

The best-fit parameter values from the spectral modeling of the 56 observations (listed in Table 2) are consistent within the uncertainties of those derived from just the 110 ks targeted observations (given in Figure 3). The addition of the serendipitous data yields smaller error bars on all of the parameters, most notably on the Ne, Si, and Fe abundances. In the arc, the uncertainties are small enough to exclude an ISM origin with $>99\%$ confidence for the Ne, Fe, and Si, suggesting these metals are ejecta material. In the bar, we also find statistically significant enhancement of Ne and Fe. Furthermore, we investigated the O abundance in the bar and arc, but we are unable to set useful constraints or upper limits on the O abundance due to absorption toward SNR 0104–72.3.

We note some caveats about the above spectral analyses. We have combined spectra from 56 observations using the CIAO command *combine_spectra*, which co-adds imaging source and background spectra as well

as instrument response files. To limit systematics, we have used the same source and background regions between observations. However, the different background rates between observations, dependent on which chip SNR 0104–72.3 falls and the off-axis distance during each observation, causes some observations to be weighted more than others. In this procedure, the two ACIS-S3 observations totaling 110 ks would be weighted most heavily, yielding results similar to those derived by the two observations alone, but with smaller error bars. Furthermore, although simultaneous fitting of the individual 56 spectra would seem optimal, in practice the procedure gave unphysical results (e.g., temperatures ~ 10 keV) as the fits found local minima of chi-squared space.

4. DISCUSSION AND CONCLUSIONS

In addition to the morphological evidence that SNR 0104–72.3 was a jet-driven CC explosion, we can further constrain the explosive origin by comparing the ejecta abundances derived from the arc and bar to those predicted by SN models. Recall the above abundances are by number relative to solar. Converting the abundance ratios to be relative to mass and propagating the uncertainties, we have $\text{Ne/Fe} = 3.4^{+1.0}_{-0.8}$ for the bar and $\text{Ne/Fe} = 3.1^{+1.2}_{-1.0}$ and $\text{Si/Fe} = 0.9 \pm 0.3$ for the arc. By comparison, Type Ia SNe produce much less Ne than we find in SNR 0104–72.3: the chemical yield of Type Ia SN models is $\text{Ne/Fe} \sim 0.006$ in the deflagration case (model W7 of Nomoto et al. 1984) or $\text{Ne/Fe} \sim 0.001$ in the delayed detonation case (model WDD2 of Nomoto et al. 1997). In contrast, the massive progenitors of CC SNe produce several orders of magnitude more Ne than Type Ia SNe, and thus they are more consistent with our measured ejecta abundances. In particular, the Ne/Fe ratio of the spherical CC models of Nomoto et al. (2006) increases with progenitor mass, from $\text{Ne/Fe} \sim 1.8$ for a $13 M_{\odot}$ progenitor to $\text{Ne/Fe} \sim 25$ for a $40 M_{\odot}$ progenitor (for a $1/5$ solar metallicity star). Figure 5 shows graphically how our results compare to the values given by the models. The Ne/Fe ratios of the arc and bar of SNR 0104–72.3 are most similar to the model predictions of the 18–20 M_{\odot} progenitors, which have $\text{Ne/Fe} \sim 2.3$ and ~ 3.7 , respectively. Our Si/Fe from the arc is also consistent with a 18–20 M_{\odot} progenitor, as the spherical CC

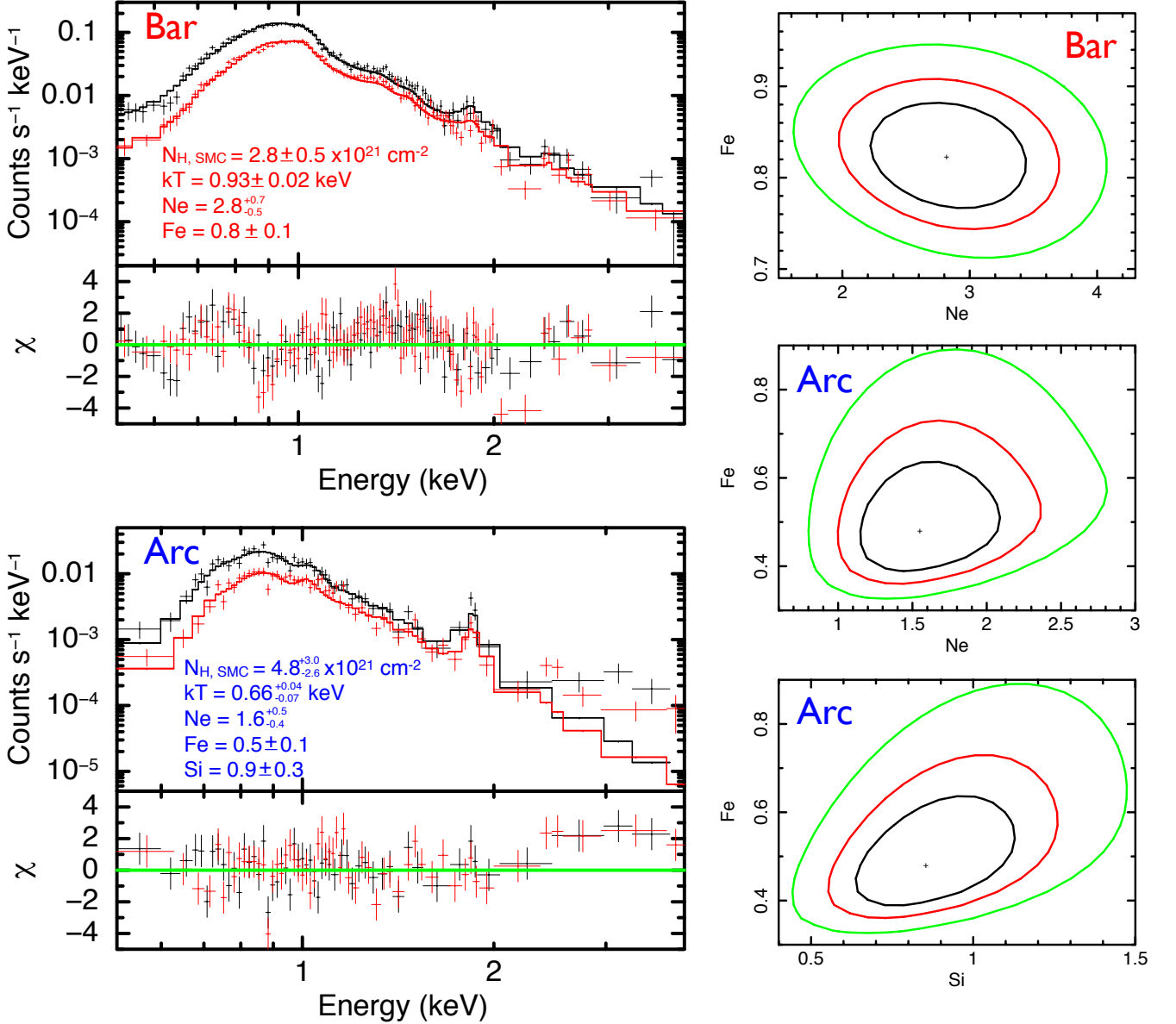


FIG. 4.— Spectral analyses of the bar and arc from all 56 *Chandra* ACIS observations of SNR 0104–72.3. *Top left*: Back-illuminated (BI) and front-illuminated) spectra and model in black and red, respectively, of the bar region. *Bottom left*: Same as top except for the arc region of SNR 0104–72.3. *Right panels*: 68%, 95%, and 99% confidence contours of Fe versus Ne abundances in the bar (top), of Fe versus Ne abundances in the arc (middle), and of Fe vs Si abundances in the arc (bottom). All abundances are relative to solar by number. In the bar, we find enhanced abundances of Fe and Ne, and in the arc, we find enhanced abundances of Ne, Si, and Fe. Using all 56 observations, we find that the abundances of these elements in the arc and bar are enhanced, indicating an ejecta origin.

model gives $\text{Si}/\text{Fe} \sim 1.0\text{--}1.7$.

Given the elliptical/elongated morphology of SNR 0104–72.3, we also compare the abundance results to model predictions of aspherical CC SNe. Maeda & Nomoto (2003) predict Ne/Fe ratios similar to those we obtain in the arc and bar, ranging from $\text{Ne}/\text{Fe} \sim 4\text{--}7$ in their aspherical models of $25 M_{\odot}$ and $40 M_{\odot}$ progenitors (their models 25A, 25B, 40A, and 40B). However, the Si/Fe of the arc is below the yields of the aspherical $40 M_{\odot}$ models (which give $\text{Si}/\text{Fe} \sim 2.1$). Thus, our best-fit abundances are most consistent with either a spherical CC SN of a $18\text{--}20 M_{\odot}$ progenitor or an aspherical CC SN of a $25 M_{\odot}$ progenitor. Of these two possible progenitors, we favor an aspherical explosion

scenario for SNR 0104–72.3 due to its highly elliptical morphology. We also emphasize that hydrodynamical modeling of SNe has only sampled a small subset of the parameter space that can affect nucleosynthesis (e.g., jet opening angles, explosion energy, progenitor mass and metallicity). As such, our constraints on the progenitor mass from the metal abundances should be interpreted as approximate rather than as strict limits.

Here, we have assumed that all of the ejecta has been shock-heated and is well mixed, and thus, the best-fit abundances reflect the nucleosynthetic yield of the SN explosion. We can justify this assumption based on the age t of SNR 0104–72.3, using the Sedov-Taylor solution:

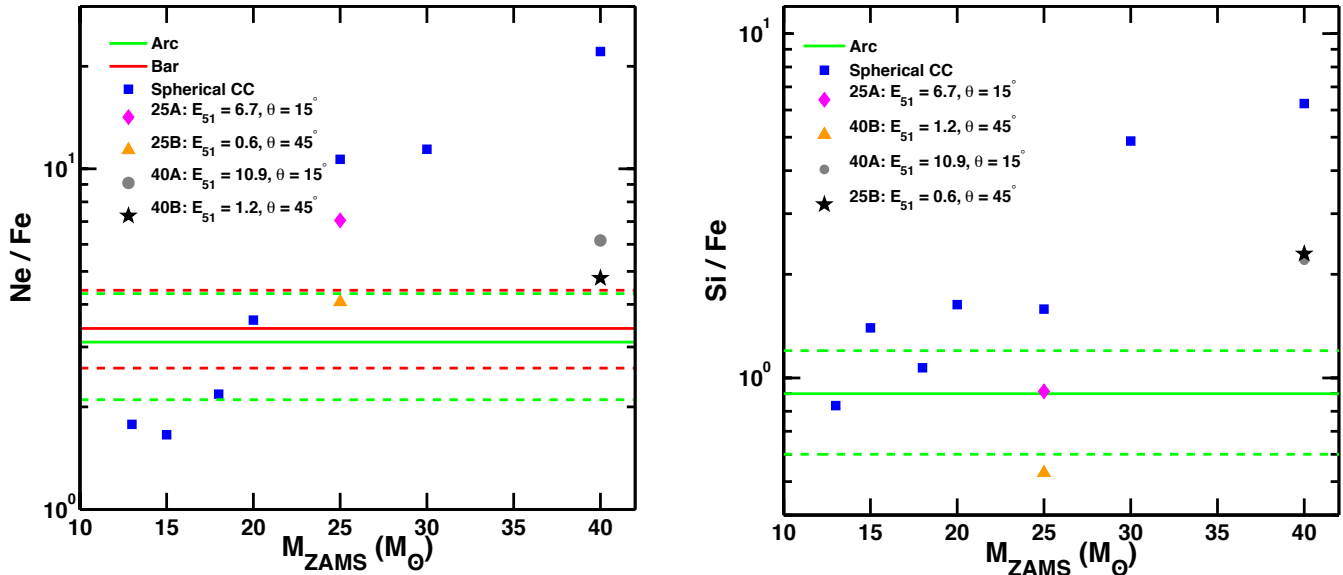


FIG. 5.— Plots comparing the derived abundance ratios Ne/Fe (left) and Si/Fe (right) of SNR 0104–72.3 to those predicted by CC SN models. Solid lines represent the best-fit values for the arc (light green) and the bar (red), with the dashed lines reflecting the $1\text{-}\sigma$ uncertainties of those estimates. For comparison, we show the ratios produced by spherical CC models for different zero-age main-sequence mass stars M_{ZAMS} (blue squares, from Nomoto et al. 2006) and aspherical CC models of $25 M_{\text{ZAMS}}$ (purple diamond and black star) and $40 M_{\text{ZAMS}}$ (gray circle and stars from Maeda & Nomoto 2003).

$$t = 17.3 \left(\frac{10^{51} \text{ erg}}{E_{\text{SN}}} \right)^{1/2} \left(\frac{n_0}{1.0 \text{ cm}^{-3}} \right)^{1/2} \left(\frac{R_s}{1 \text{ pc}} \right)^{5/2} \text{ years.} \quad (1)$$

The diameter of SNR 0104–72.3 is $\sim 1.8'$, corresponding to $R_s \sim 16$ pc, assuming a distance of 61 kpc to the SMC (Hilditch et al. 2005). Given this radius, the approximate age of SNR 0104–72.3 is $t \sim 17600$ years, for an explosion of energy $E_{\text{SN}} = 10^{51}$ erg in an ambient electron density of $n_0 = 1.0 \text{ cm}^{-3}$. At this relatively evolved stage, the reverse shock would have completed its propagation inward relative to the ejecta (see Truelove & McKee 1999), heating the ejecta to X-ray emitting temperatures.

In this paper, we have employed 528.6 ks of serendipitous *Chandra* observations to reconsider the explosive origin of the SMC SNR 0104–72.3. We have demonstrated that the X-ray morphology of SNR 0104–72.3 is extremely elliptical/elongated compared to other young SNRs in the MW and the LMC, suggesting it is the result of a core-collapse SN. Furthermore, we have performed spectral modeling of two regions of SNR 0104–72.3, and we have found enhanced abundances of Ne, Si, and Fe. Through comparison to the nucleosynthesis predictions of Type Ia and CC SN models, we demonstrate that the yields are consistent with either a spherical CC SN of a $18\text{--}20 M_{\odot}$ progenitor or an aspherical CC SN of a $25 M_{\odot}$ progenitor. Given the bipolar morphology of the SNR, we consider the latter scenario to be more likely, in which case it would be the second SNR likely to have had a bipolar origin (the first being W49B in the MW; Lopez et al. 2013b).

As a consistency check on the nature of SNR 0104–72.3, we investigate the star formation history (SFH) at the site of SNR 0104–72.3 using the

spatially-resolved SFH maps of the SMC produced by Harris & Zaritsky (2004). These authors obtained *UBVI* photometry of 6 million stars across the SMC and produced a uniform grid of $12' \times 12'$ regions, each with its own SFH derived from StarFISH (Harris & Zaritsky 2001). Figure 6 shows a plot of the star formation rate (SFR) versus age obtained by Harris & Zaritsky at the location of SNR 0104–72.3. The peak SFR occurred at ~ 7 Myr ago for a metallicity $Z = 0.004$ or at ~ 15 Myr ago for $Z = 0.008$. These ages correspond to stars of zero-age main sequence mass $M_{\text{ZAMS}} \sim 30 M_{\odot}$ or $M_{\text{ZAMS}} \sim 13 M_{\odot}$, respectively, using the single star models of Eldridge et al. (2008). Thus, the SFH at the site of SNR 0104–72.3 – particularly that of the low-metallicity case – gives the appropriate age for a massive star ($\sim 25\text{--}40 M_{\odot}$) origin of SNR 0104–72.3. Although the averaged SFHs derived from resolved stellar populations can be misleading regarding SN progenitors (especially for Type Ia SNRs; see the discussion of Badenes et al. 2009), this approach provides a complementary means to verify our results.

The identification of a bipolar SNR in the SMC is remarkable given that only ~ 25 SNRs are known in the SMC (Badenes et al. 2010). By comparison, only one SNR in the MW has been shown to be bipolar to date (Lopez et al. 2013b) out of ~ 300 SNRs (Green 2009), an order of magnitude larger sample. Yet if the SN rate is proportional to the star formation rate (SFR) of a galaxy, then the number of bipolar SNe in the MW should be a factor of 20 *greater* than the SMC (assuming a SFR of $\sim 1 M_{\odot} \text{ year}^{-1}$ in the MW and of $\sim 0.05 M_{\odot} \text{ year}^{-1}$ in the SMC; Wilke et al. 2004; Robitaille & Whitney 2010). Thus, a bipolar SNR in the SMC may suggest that jet-driven explosions may occur more commonly in the SMC, a low metallicity galaxy (with $\sim 0.2 Z_{\odot}$; Russell & Dopita 1992). If bipolar SNe happened at the

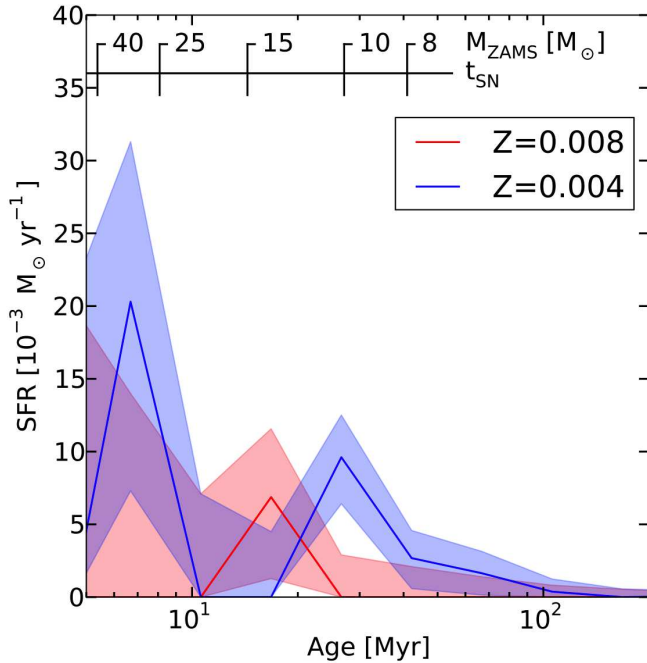


FIG. 6.— Star formation rate (SFR) versus look-back time for two metallicity stellar populations ($Z = 0.004$ and $Z = 0.008$) at the site of SNR 0104–72.3, taken from the star-formation history (SFH) maps of the SMC produced by Harris & Zaritsky (2004). The solid lines represent the best-fit SFR reported by Harris & Zaritsky (2004), and the shaded regions give their 68% confidence limits. At the top of the figure, we mark the time t_{SN} when the progenitor star of a given zero-age main sequence mass M_{ZAMS} would have formed (using the single star models of Eldridge et al. 2008). We find that the peak SFR occurred at ~ 7 Myr ago for a metallicity $Z = 0.004$ or at ~ 15 Myr ago for $Z = 0.008$. These ages correspond to progenitor stars of mass $M_{\text{ZAMS}} \sim 30M_{\odot}$ or $M_{\text{ZAMS}} \sim 13M_{\odot}$, respectively. Thus, the SFH at the site of SNR 0104–72.3 is also suggestive of a CC origin of this SNR.

same rate in the MW and SMC, we would expect to have ~ 12 bipolar SNRs out of the 300 in our galaxy. While no other MW SNRs currently show evidence of bipolarity (based on e.g., morphology, abundances, and star-formation histories: Lopez et al. 2011), a full statistical analysis is necessary to demonstrate definitively

that bipolar SNe are more likely in the SMC compared to the MW.

If this result holds, it is consistent with recent work showing bipolar SNe prefer low-metallicity environments (e.g., Ramirez-Ruiz et al. 2002; Izzard et al. 2004; Fruchter et al. 2006), since rapid rotation without extensive mass loss is required to produce these explosions. In particular, broad-line (BL) Type Ic SNe (which are thought to be jet-driven explosions) are observed to occur at lower median metallicity than typical Type Ib/c SNe (Sanders et al. 2012). Furthermore, at sufficiently low metallicity (~ 0.2 – $0.6 Z_{\odot}$), BL-Ic SNe are associated with long-duration GRBs (Kaneko et al. 2007; Modjaz et al. 2008), and 75% of long GRBs are located in host galaxies with $\lesssim 0.5 Z_{\odot}$ (Graham & Fruchter 2013). Our findings would support this framework of jet-driven explosions happening more frequently at low metallicity.

In the future, Astro-H observations of SNR 0104–72.3 will be able to differentiate the Ne and Fe L emission lines that comprise the bump in the X-ray spectra at 0.9–1.1 keV, facilitating tighter constraints on the relative abundances of the two elements. Although the distance to the SMC would preclude the X-ray detection of a thermal emission from any central compact object, non-thermal emission or pulsations may be observable if the SNR has a pulsar.

We acknowledge helpful discussions with J.-J. Lee in writing this paper. Support for LAL was provided by NASA through the Einstein Fellowship Program, grant PF1–120085, and the MIT Pappalardo Fellowship in Physics. ERR acknowledges support from the David and Lucile Packard Foundation and NSF grant AST–0847563. DC and POS acknowledge support for this work provided by NASA through the Smithsonian Astrophysical Observatory contract SV3–73016 to MIT for support of the Chandra X-ray Center, which is operated by the Smithsonian Astrophysical Observatory for and on behalf of NASA under contract NAS8–03060.

REFERENCES

- Anders, E., & Grevesse, N. 1989, *Geochim. Cosmochim. Acta*, 53, 197
- Arnaud, K. A. 1996, in *Astronomical Society of the Pacific Conference Series*, Vol. 101, *Astronomical Data Analysis Software and Systems V*, ed. G. H. Jacoby & J. Barnes, 17
- Asplund, M., Grevesse, N., Sauval, A. J., & Scott, P. 2009, *ARA&A*, 47, 481
- Aubourg, E., Tojeiro, R., Jimenez, R., Heavens, A., Strauss, M. A., & Spergel, D. N. 2008, *A&A*, 492, 631
- Badenes, C., Hughes, J. P., Bravo, E., & Langer, N. 2007, *ApJ*, 662, 472
- Badenes, C., Harris, J., Zaritsky, D., & Prieto, J. L. 2009, *ApJ*, 700, 727
- Badenes, C., Maoz, D., & Draine, B. T. 2010, *MNRAS*, 407, 1301
- Borkowski, K. J., Lyerly, W. J., & Reynolds, S. P. 2001, *ApJ*, 548, 820
- Dan, M., Rosswog, S., Guillochon, J., & Ramirez-Ruiz, E. 2012, *MNRAS*, 422, 2417
- Dickey, J. M., & Lockman, F. J. 1990, *ARA&A*, 28, 215
- Eldridge, J. J., Izzard, R. G., & Tout, C. A. 2008, *MNRAS*, 384, 1109
- Foster, A. R., Ji, L., Smith, R. K., & Brickhouse, N. S. 2012, *ApJ*, 756, 128
- Fruchter, A. S., et al. 2006, *Nature*, 441, 463
- Gehrels, N., Ramirez-Ruiz, E., & Fox, D. B. 2009, *ARA&A*, 47, 567
- González-Casanova, D. F., De Colle, F., Ramirez-Ruiz, E., & Lopez, L. A. 2014, *ApJ*, 781, L26
- Graham, J. F., & Fruchter, A. S. 2013, *ApJ*, 774, 119
- Green, D. A. 2009, *Bulletin of the Astronomical Society of India*, 37, 45
- Guillochon, J., Dan, M., Ramirez-Ruiz, E., & Rosswog, S. 2010, *ApJ*, 709, L64
- Harris, J., & Zaritsky, D. 2001, *ApJS*, 136, 25
- Harris, J., & Zaritsky, D. 2004, *AJ*, 127, 1531
- Hilditch, R. W., Howarth, I. D., & Harries, T. J. 2005, *MNRAS*, 357, 304
- Iben, Jr., I., & Tutukov, A. V. 1984, *ApJS*, 54, 335
- Izzard, R. G., Ramirez-Ruiz, E., & Tout, C. A. 2004, *MNRAS*, 348, 1215
- Kaneko, Y., Ramirez-Ruiz, E., Granot, J., et al. 2007, *ApJ*, 654, 385

- Kerzendorf, W. E., Childress, M., Scharwaechter, J., Do, T., & Schmidt, B. P. 2013, ArXiv e-prints
- Koo, B.-C., et al. 2007, PASJ, 59, 455
- Law, N. M., et al. 2009, PASP, 121, 1395
- Leaman, J., Li, W., Chornock, R., & Filippenko, A. V. 2011, MNRAS, 412, 1419
- Lee, J.-J., Park, S., Hughes, J. P., Slane, P. O., & Burrows, D. N. 2011, ApJ, 731, L8
- Lopez, L. A., Pearson, S., Ramirez-Ruiz, E., Castro, D., Yamaguchi, H., Slane, P. O., & Smith, R. K. 2013a, ArXiv e-prints
- Lopez, L. A., Ramirez-Ruiz, E., Badenes, C., Huppenkothen, D., Jeltama, T. E., & Pooley, D. A. 2009a, ApJ, 706, L106
- Lopez, L. A., Ramirez-Ruiz, E., Castro, D., & Pearson, S. 2013b, ApJ, 764, 50
- Lopez, L. A., Ramirez-Ruiz, E., Huppenkothen, D., Badenes, C., & Pooley, D. A. 2011, ApJ, 732, 114
- Lopez, L. A., Ramirez-Ruiz, E., Pooley, D. A., & Jeltama, T. E. 2009b, ApJ, 691, 875
- Maeda, K., & Nomoto, K. 2003, ApJ, 598, 1163
- Modjaz, M., et al. 2008, AJ, 135, 1136
- Nomoto, K., Iwamoto, K., Nakasato, N., Thielemann, F.-K., Brachwitz, F., Tsujimoto, T., Kubo, Y., & Kishimoto, N. 1997, Nuclear Physics A, 621, 467
- Nomoto, K., Thielemann, F.-K., & Yokoi, K. 1984, ApJ, 286, 644
- Nomoto, K., Tominaga, N., Umeda, H., Kobayashi, C., & Maeda, K. 2006, Nuclear Physics A, 777, 424
- Pakmor, R., Kromer, M., Taubenberger, S., Sim, S. A., Röpke, F. K., & Hillebrandt, W. 2012, ApJ, 747, L10
- Peters, C. L., Lopez, L. A., Ramirez-Ruiz, E., Stassun, K. G., & Figuroa-Feliciano, E. 2013, ApJ, 771, L38
- Podsiadlowski, P., Mazzali, P. A., Nomoto, K., Lazzati, D., & Cappellaro, E. 2004, ApJ, 607, L17
- Ramirez-Ruiz, E., Lazzati, D., & Blain, A. W. 2002, ApJ, 565, L9
- Ramirez-Ruiz, E., & MacFadyen, A. I. 2010, ApJ, 716, 1028
- Robitaille, T. P., & Whitney, B. A. 2010, ApJ, 710, L11
- Russell, S. C., & Dopita, M. A. 1992, ApJ, 384, 508
- Sanders, J. S., & Fabian, A. C. 2001, MNRAS, 325, 178
- Sanders, N. E., et al. 2012, ApJ, 758, 132
- Scannapieco, E., & Bildsten, L. 2005, ApJ, 629, L85
- Schaefer, B. E., & Pagnotta, A. 2012, Nature, 481, 164
- Sedov, L. I. 1959, Similarity and Dimensional Methods in Mechanics, New York: Academic Press, 1959
- Smith, R. K., Brickhouse, N. S., Liedahl, D. A., & Raymond, J. C. 2001, ApJ, 556, L91
- Smith, R. K., & Hughes, J. P. 2010, ApJ, 718, 583
- Soderberg, A. M., et al. 2010, Nature, 463, 513
- Stanimirovic, S., Staveley-Smith, L., Dickey, J. M., Sault, R. J., & Snowden, S. L. 1999, MNRAS, 302, 417
- Truelove, J. K., & McKee, C. F. 1999, ApJS, 120, 299
- Vink, J. 2012, A&A Rev., 20, 49
- Webbink, R. F. 1984, ApJ, 277, 355
- Whelan, J., & Iben, Jr., I. 1973, ApJ, 186, 1007
- Wilke, K., Klaas, U., Lemke, D., Mattila, K., Stickel, M., & Haas, M. 2004, A&A, 414, 69
- Williams, B. J., et al. 2011, ApJ, 741, 96